

https://dspace.org/

Constitutive analysis of hot metal flow behavior of virgin and rejuvenated heat treatment creep exhausted power plant x20 steel

S Maube; J Obiko; Josias Van Der Merwe; F Mwema; Desmond Klenam ...

https://hdl.handle.net/10539/40523
WOS

Downloaded from a DSpace repository. https://dspace.org/

The International Journal of Advanced Manufacturing Technology (2024) 132:1843–1853
https://doi.org/10.1007/s00170-024-13443-9

ORIGINAL ARTICLE

Constitutive analysis of hot metal flow behavior of virgin and rejuvenated heat treatment creep exhausted power plant X20 steel

Shem Maube[1] · Japheth Obiko[2] · Josias Van der Merwe[3,4] · Fredrick Mwema[1,5,6] · Desmond Klenam[3] · Michael Bodunrin[3,4]

Received: 5 November 2023 / Accepted: 13 March 2024 / Published online: 25 March 2024
© The Author(s), under exclusive licence to Springer-Verlag London Ltd., part of Springer Nature 2024

Abstract

This paper presents constitutive equations that describe the hot flow behaviour of Virgin (VG) X20 and rejuvenated heat-treated creep exhaust (CE) X20 steels. The study provides a foundation for determining the effect of rejuvenation heat treatment on CE steels by making comparisons to the VG steel. Hot compression tests were conducted in the temperature range of 900 °C to 1050 °C, at strain rates of 0.1–10 s^{-1} to a total strain of 0.6, and stress–strain curves were obtained. The flow stress curves of both steels exhibited dynamic recovery (DRV) characteristics as the main softening mechanism. Constitutive constants of steady-state stresses were determined. The stress exponents, n, were 6.62 (VG) and 5.58 (CE), and the apparent activation energy values were 380.36 $kJmol^{-1}$(VG) and 435.70 $kJmol^{-1}$ (CE). Analysis of the activation energies showed that VG steel had better workability properties than CE steel and was easier to deform at high temperatures. Constitutive equations for predicting the flow stress in the two steels were established. This were verified by statistical tools: Pearson's correlation coefficient (R) and Absolute Average Relative Error (AARE). The results showed R-values were, 0.98 (VG) and 0.99 (CE), and the AARE values for VG were 4.17% and 9.01% for CE. The statistical parameters indicated a good correlation between the experimental and predicted values. The constitutive equations therefore adequately described the flow stress behaviour of both steels and can therefore efficiently analyse industrial metal forming schedules.

Keywords X20 · Rejuvenation · Hot Deformation · Heat Treatment · Constitutive Analysis

1 Introduction

Martensitic–ferritic 9–12% Cr steels are widely used for creep-resistant components operating at elevated temperatures in steam power-generating plants [1]. One of the 9–12% Cr steels, that operate at the creep range in thermal and steam power generation is the X20CrMoV12-1 steel (hereby referred to as X20). X20 has been extensively used since the 1960s for tubes and pipework of thermal power plants operating at temperatures of up to 565 °C [2]. This steel exhibits high creep strength, excellent corrosion, and fatigue resistance [3–6].

The Creep strength of X20 steel is obtained from solid solution hardening and precipitation strengthening. Before service, the steel components undergo a heat treatment procedure of austenitisation followed by air cooling, and tempering [7]. After heat treatment, the microstructure of the X20 steel is tempered martensite with precipitates along grain boundaries [8, 9]. Some of the precipitates are the

✉ Shem Maube
smaube@gmail.com

1 Department of Mechanical Engineering, Dedan Kimathi University of Technology, Nyeri, Kenya

2 Department of Mining, Materials and Petroleum Engineering, Jomo Kenyatta University of Agriculture and Technology, Nairobi, Kenya

3 School of Chemical and Metallurgical Engineering, Faculty of Engineering and the Built Environment, University of the Witwatersrand, Johannesburg, South Africa

4 DSI-NRF Centre of Excellence in Strong Materials, University of the Witwatersrand, Johannesburg, South Africa

5 Department of Mechanical and Construction Engineering, Northumbria University, Newcastle, UK

6 Department of Mechanical Engineering Science, University of Johannesburg, Johannesburg, South Africa

carbides of the precipitates, such as $M_{23}C_6$, M_7C_3, M_2X, and MX [2]. In the X20CrMoV12-1 steel, $M_{23}C_6$ carbides (M = Cr, Mo) produce the main creep-strengthening mechanisms by precipitating along the sub-grain interior while, MX (M = V, N) carbonitrides precipitate in the matrix enhancing high-temperature stability during service [9]. Further strengthening is provided by grain refinement from the formation of the tempered martensite structure with high dislocation density and high Cr and Mo providing solid solution strengthening [3].

Long-term exposure of the X20 steam pipes in thermal plants at creep temperatures causes changes to the microstructure and carbide morphology resulting in material exhaustion [10]. The changes induced during service include, softening of the martensite matrix, change in the precipitation composition, the disappearance of prior austenite grain boundaries (PAGB), formation of sub-grains, and emergence of undesirable secondary phases, such as the Z phase [11–13]. The Z-phase (Cr (V, Nb) N) is similar in chemical elements to MX (Metal: V, Nb, and X: N) precipitates, with the only difference being chromium [13].

During service, the MX particles transform into the more stable and relatively coarse Z-phase [14]. This causes large spacing between particles hence lower creep strength [15]. The presence of higher chromium content in X20 steel (up to 12% Cr) further accelerates the precipitation of the Z-phase, causing microstructural degradation [9]. The evolution of microstructure during service therefore causes degradation of mechanical properties and shorter operational periods.

After a failure or end of design life, the X20 pipes are decommissioned and scraped. The high costs involved in the replacement of pipes have generated an increased industrial interest in prolonging the operational life of the exhaust steel [16]. Researchers have suggested the rejuvenation heat treatment process for restoring the properties and microstructure of creep-exhausted metals and alloys to their original condition [4, 17–19]. In this case, a two-stage heat treatment process: normalisation and tempering (N + T), has been suggested by researchers [11, 20]. During the normalisation process, the dissolution of microstructural phases occurs, forming a single-phase microstructure [20]. After tempering, the desired microstructure is achieved thus enhancing solid solution strengthening [12]. Previous studies on 12 wt.% Cr steels have focused on the effects of rejuvenation heat treatment on mechanical properties and microstructure evolution of aged power plant steels [6, 20, 21]. However, the literature on metal flow behaviour and constitutive modelling of rejuvenated heat-treated creep-exhausted steels X20 steel is conspicuously missing in the literature. In this study rejuvenation heat treatment procedure of normalising and tempering was applied to 100,000 h (CE) X20 steel. Hot compression testing was conducted using a Gleeble® 3500 thermal–mechanical simulator on the CE steel and VG steel, which was the control sample under the same conditions. Constitutive equations were then developed to explore the hot flow behaviour of the two steels and evaluate their suitability to predict flow stress through statistical methods.

2 Experimental procedure

The materials in this study were obtained from virgin and creep-exhausted X20 steels for steam pipes. The microstructures of the steels are shown in Fig. 1 a) VG and b) CE. The micrograph of the VG steel shows tempered lath martensite with parallel lath boundaries inside the PAGBs. The microstructure of the CE steel shows the effects of prolonged service conditions. The carbides at the grain boundaries and former austenite boundaries are distinctively coarser and PAGBs are more discernible. The chemical composition (wt%) of the pipes are shown in Table 1. For hot compression testing, cylindrical test samples of 12 mm height and diameter of 8 mm were cut from sections of each pipe using an Electro-discharge Machine (EDM) wire cutter. From each steel, 12 test sample pieces were machined, hence

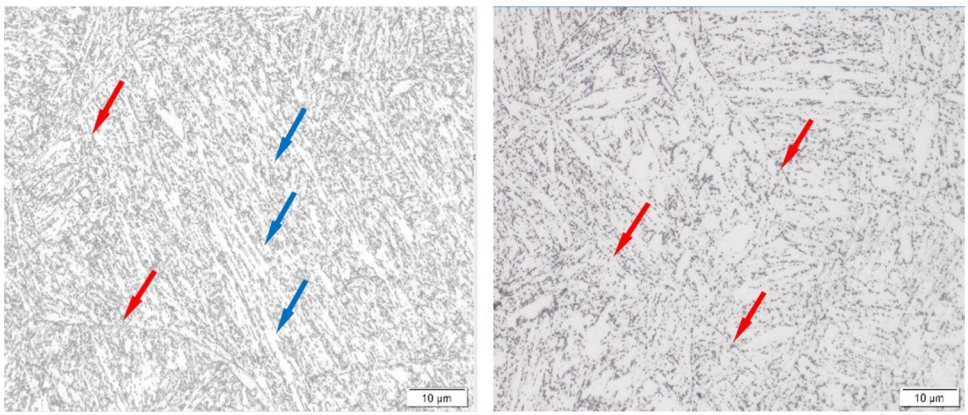

a) b)

Fig. 1 Optical micrographs of the **a**) VG steel and **b**) CE steel. (Red arrows indicate PAGBs, Blue arrows show the parallel laths boundaries in PAGBs)

Table 1 Chemical composition of X20 the steels

Elements	Mn	C	Cr	P	Ni	Mo	V	Cu	W	Nb
(wt.%)	0.46	0.198	11.35	0.02	0.648	0.909	0.259	0.086	0.01	0.76

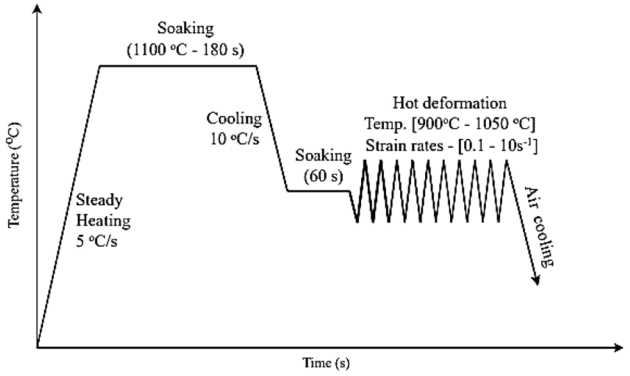

Fig. 2 The thermal history of hot compression test

a total of 24 test pieces. Samples from the CE steel were subjected to rejuvenation heat treatment by normalising at 1050 °C for 40 min, air-cooling, and tempering at 760 °C for 120 min. Using a Gleeble®3500 thermo-mechanical simulator, hot compression tests were conducted on each test sample following the schedule shown in Fig. 2. The test conditions were distributed in a 3×4 matrix for 12 variations of the test. The test conditions were strain rates of 0.1 s^{-1}, 1 s^{-1} and 10 s^{-1}; the temperatures at each strain rate were 900 °C, 950 °C, 1000 °C, and 1050 °C. All deformations were conducted to a total strain of 0.6.

During the hot compression testing, friction was experienced at the anvil and test piece interface. A graphite foil sprayed with nickel paste was therefore applied to lubricate the contacting surfaces. The friction was however not entirely eliminated especially at high strain rate. This caused inhomogeneous flow of material with the test piece bulging at the mid-section in a phenomenon called 'barrelling'. The flow stress data were therefore inaccurate and the flow curves had to be corrected. The barrelling coefficient, b for each deformed test piece was determined using Equation (1) [21] by considering the sample geometry. The allowable range was $1 < b \leq 1.1$ as the effect of friction within these limits were considered to be negligible [22]. Samples with b greater than 1.1 were considered invalid and flow curves of the corresponding test samples corrected using Equation (4) [23]:

$$b = 4\frac{(r_m - r_t)}{r_a}\frac{h}{(h - h_o)} \tag{1}$$

where r_m is the radius of the sample after deformation, r_a is the theoretical radius given by Equation (2), r_t is the top radius given by Equation (3), r_o is the initial radius, h_o is the initial height, and h is the height of the sample after deformation.

$$r_a = r_o\sqrt{\frac{h_o}{h}} \tag{2}$$

$$r_t = \sqrt{3\frac{h_o}{h}r_o^2 - 2r_m^2} \tag{3}$$

$$\widetilde{\sigma} = \frac{\sigma_a}{1 + \left(\frac{2}{3\sqrt{3}}\right)m\left(\frac{r_o}{h_o}\right)exp\left(\frac{3\widetilde{\varepsilon}}{2}\right)} \tag{4}$$

$\widetilde{\sigma}$ is flow stress after correction, σ_a is experimental flow stress, $\widetilde{\varepsilon}$ is the measured instantaneous strain, m is the average friction factor given by Equation (5) [24], it ranges between 0 (perfect sliding) to 1 (sticking friction) [24]:

$$m = \frac{\left(\frac{r_a}{h}\right)b}{\left(\frac{4}{\sqrt{3}}\right) - \left(\frac{2b}{3\sqrt{3}}\right)} \tag{5}$$

3 Results and discussion

3.1 Flow stress–strain curves

The flow stress data generated by the Gleeble 3500® thermo-mechanical simulator was inaccurate as it was acquired under ideal conditions. The system did not account for the effect of friction occurring between the anvil and the sample. This caused inhomogeneous deformation preventing radial flow of material and barrelling of the sample. The stresses recorded when barrelling occurred were therefore higher than the actual stress values. The stress–strain curves of the steels were hence corrected for the effect of friction. Figure 3 shows a select plot of uncorrected and friction-corrected stress–strain curves of the VG and CE steels at a temperature of 950 °C and strain rate of 1 s^{-1}.

Figures 4 and 5 are the friction-corrected stress–strain curves obtained from hot compression testing for all conditions of deformation for the VG and CE steels. As seen, both steels exhibit similar flow stress behaviour and are sensitive to the deformation temperature and strain rate. At a constant strain rate, the flow stresses decrease with an increase in the temperature of deformation. This is attributed to the increase in deformation temperature which causes an increase in the

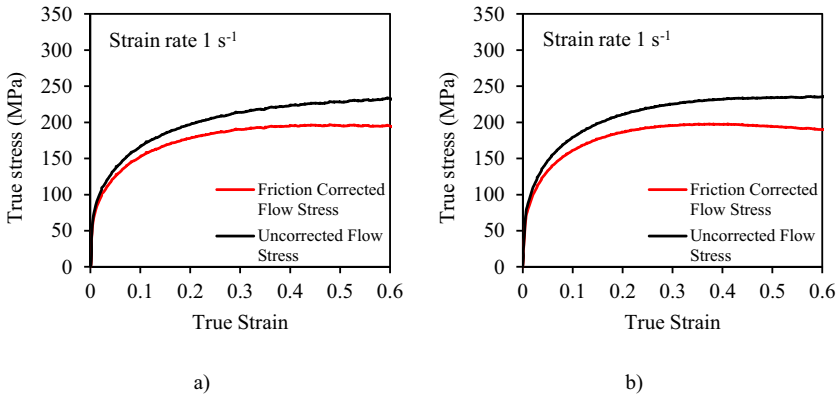

Fig. 3 Stress–strain curves showing friction corrected and uncorrected curves of a) VG and b) CE steels

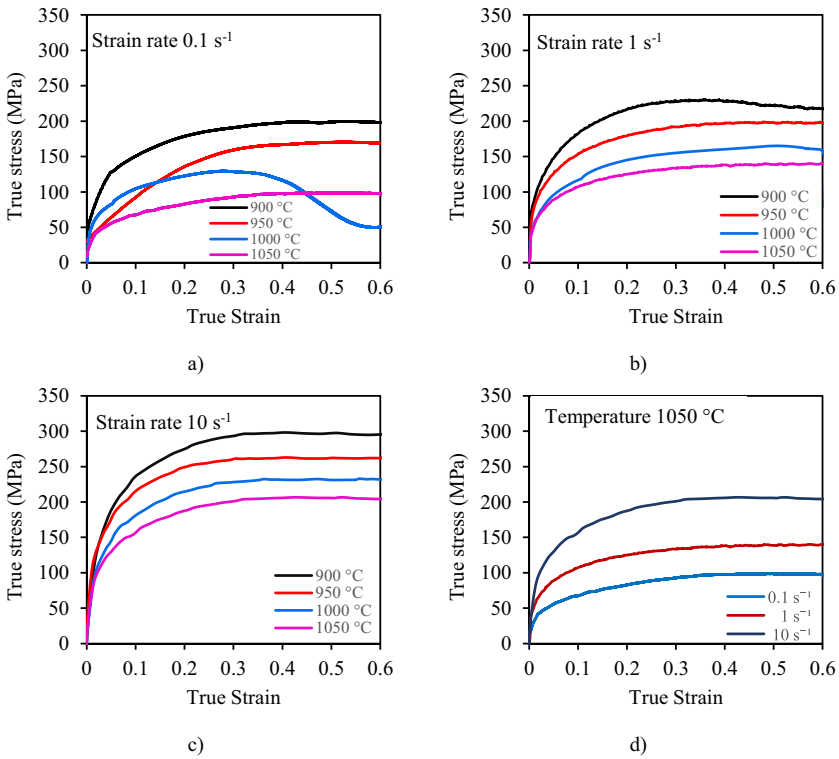

Fig. 4 Flow stress–strain curves for VG steel at different strain rates and temperatures

rate of vacancy diffusion, climb of edge dislocations, and cross-slip of screw dislocations [24–26]. In the early stages (at strains < 0.2), work hardening prevails the deformation mechanisms causing a rapid increase in the dislocation density. The high dislocation density resists the deformation process, causing an increase in the flow stress. As the deformation progresses (to strains > 0.2), the flow stress curves display limited work hardening due to the increased softening effect. The decrease in flow stress progresses until the effect of work hardening and dynamic softening reaches an equilibrium. At this stage, the flow stress curves show steady-state flow stress where there is a relatively constant dislocation density. This characteristic flow behaviour suggests that DRV is the main softening mechanism [27].

At constant temperature, the flow stress increases as the strain rate increases. Deformation at a higher strain rate causes a higher rate of dislocation multiplication, resulting in the dislocation-strengthening effect. This phenomenon causes higher resistance to deformation due to work hardening, which controls the deformation process at a high strain rate. This, therefore, causes deformation difficulties resulting in higher flow stresses [28]. During deformation at low strain rates, there is more time for dynamic recovery to occur, hence weakening the effect of work hardening. This relationship is observed in both steels at all temperatures and illustrated by Fig. 4 d) for VG and Fig. 5 d) at 1050 °C.

Flow stress–strain curves reflect the effect of deformation conditions on the microstructure. Microstructural changes are

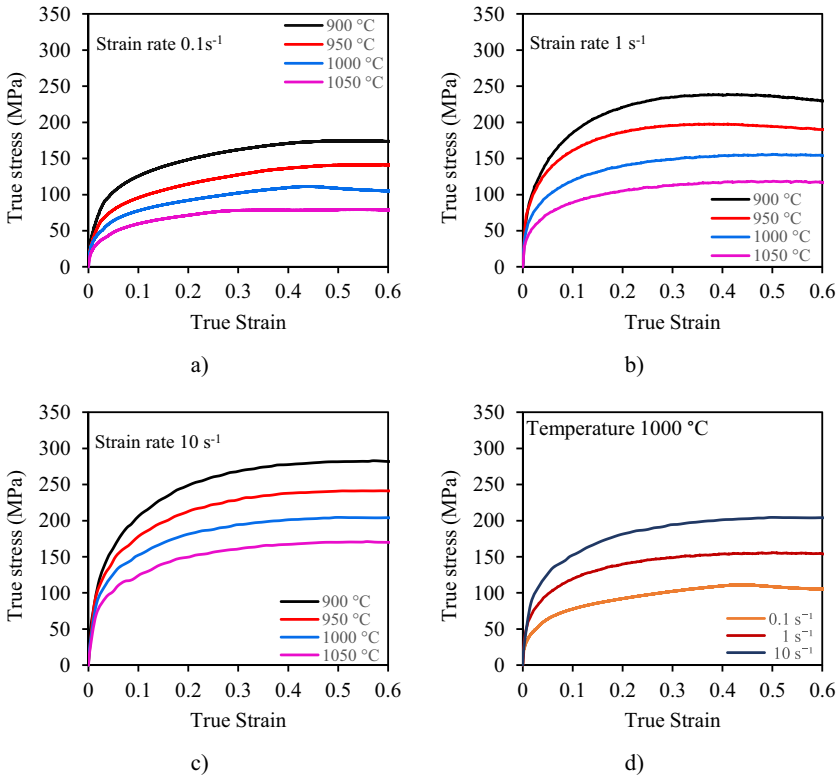

Fig. 5 Flow stress–strain curves of CE steel at different strain rates and temperatures

related closely to the deformation mechanisms controlling the metal flow behaviour during hot forming [29]. Work hardening (WH) and flow softening mechanisms, such as dynamic recrystallization (DRX) and DRV, are reliant on the parameters during forming. The main flow softening mechanism of creep-resistant steels such as X20 with high stacking fault energy is DRV. During deformation, these steels easily re-arrange into polygonal sub-grain structures by dislocation climb and cross-slip, resulting in DRV[30]. The flow stress curves in Fig. 4 for VG and Fig. 5 for CE exhibited similar flow behaviour. It was observed that at strains below 0.2, WH dominated the deformation, and above 0.2, the curves exhibited DRV softening mechanisms until the end of the deformation process. This result implies that the hot working of the rejuvenated heat treatment CE steels within the temperature range of 950–1100 °C, would allow the recycling of the steel by hot deformation into new components with comparable flow characteristics of the virgin steel.

3.2 Flow stress curve modelling

3.2.1 Constitutive modelling

Constitutive equations are applied widely in the analysis of metal flow behaviour for various metals and alloys during deformation [30–33]. These equations form a basis for developing models that are used to predict flow stress behaviour at all deformation conditions [34]. For example, the Arrhenius equation is widely applied to describe the relationship between flow stress (σ), strain rate ($\dot{\varepsilon}$), and temperature (T) [34–37].

$$\dot{\varepsilon} = \mathrm{Af}(\sigma)\exp\left(\frac{-\mathrm{Q}}{\mathrm{RT}}\right) \tag{6}$$

$$\mathrm{f}(\sigma) = \begin{Bmatrix} \mathrm{A}\sigma^{\mathrm{n}'} & \text{fow low stress } \alpha\,\sigma < 0.8 \\ \mathrm{A}\ \exp\ (\beta'\sigma) & \text{fow high stress } \alpha\,\sigma < 1.2 \\ \mathrm{A}[\sinh\,(\alpha\sigma)]^{\mathrm{n}} & \textit{for} \text{ all stress } \sigma \end{Bmatrix} \tag{7}$$

From Equations (6) and (7), Q is the activation energy for deformation in kJ/mol, and R is the universal gas constant [8.3145 J/(mol. K)]. A, β, n', σ, and n are material constants. α is the stress multiplier. The constitutive constants and activation energy are derived using the general case of the Arrhenius equation [38]. Substituting f (σ) values into Equations (6) and taking natural logarithms on either side gives:

$$\ln\dot{\varepsilon} = \ln A - \frac{Q}{RT} + n'\ln\sigma \tag{8}$$

$$\ln\dot{\varepsilon} = \ln A - \frac{Q}{RT} + \beta\sigma \tag{9}$$

$$\ln\dot{\varepsilon} = \ln A - \frac{Q}{RT} + n\ln Sinh(\alpha\sigma) \tag{10}$$

Material constants were obtained using the saturation stress (Q_{sat}) in the Arrhenius type equation [39]. The saturation flow stresses were obtained directly from the stress vs strain curves at the steady-state flow stress value [31, 40]. The values of n' and β were obtained from slopes of plots of (ln (ε̇) against ln σ), and (ln (ε̇) against σ) as presented in Fig. 6 a) – b) (VG) and Fig. 7 a) – b) (CE). The stress multiplier is obtained from α = β / n [41]. n (∂ ln ε̇ against ∂ ln (sinh (ασ)) and S (∂ ln (sinh (ασ) against ∂ (1/T)) are obtained from average slope values of graphical plots of ln ε̇ against ln (sinh (ασ)) and 1000/T against ln (sinh (ασ)), as shown in Fig. 6 (c—d) for VG and Fig. 7 (c—d) for CE. By differentiating Equation (10) the activation energy is obtained as follows [42]:

$$Q = RnS = R\left[\frac{\partial\ln\dot{\varepsilon}}{\partial\ln[\sinh(\alpha\sigma)]}\right]_T\left[\frac{\partial\ln[\sinh(\sigma\sigma)]}{\partial\left({}^{1}/_{T}\right)}\right]_{\varepsilon} \tag{11}$$

3.2.2 Zener-Hollomon parameter analysis

The effects of strain rate and temperature on hot deformation behaviour relate well with Zener -Hollomon parameter Z [37, 41]. This parameter characterises the influence of deformation conditions (strain rate and temperature) on the workability of the metals and alloys. The Z-parameter is as Equation (12) [43].

$$Z = \dot{\varepsilon}\exp\left(\frac{Q}{RT}\right) = A[\mathrm{Sinh}(\alpha\sigma)]^n \tag{12}$$

Taking logarithms on either side of Equation (9), the equation may be written as follows.

$$\ln Z = \ln A + n\ln[\sinh(\alpha\sigma)] \tag{13}$$

By substituting values of Q into Equation (12), the value of Z can be obtained. The linear relationship between ln Z against ln [sinh (αα)] is shown in Fig. 8 a) for VG and b) for CE. The correlation index, R^2 for VG (0.98) and CE (0.99) shows a highly linear relationship between ln Z and ln [sinh (ασ)] in both steels. The high R^2 values for the test conditions suggested that a single deformation mechanism controlled the process. *ln A* was obtained as the intercept of the plot of ln Z vs ln [sinh (αα)]. Table 2 is a summary of constitutive constants and activation energies of the VG and CE steels.

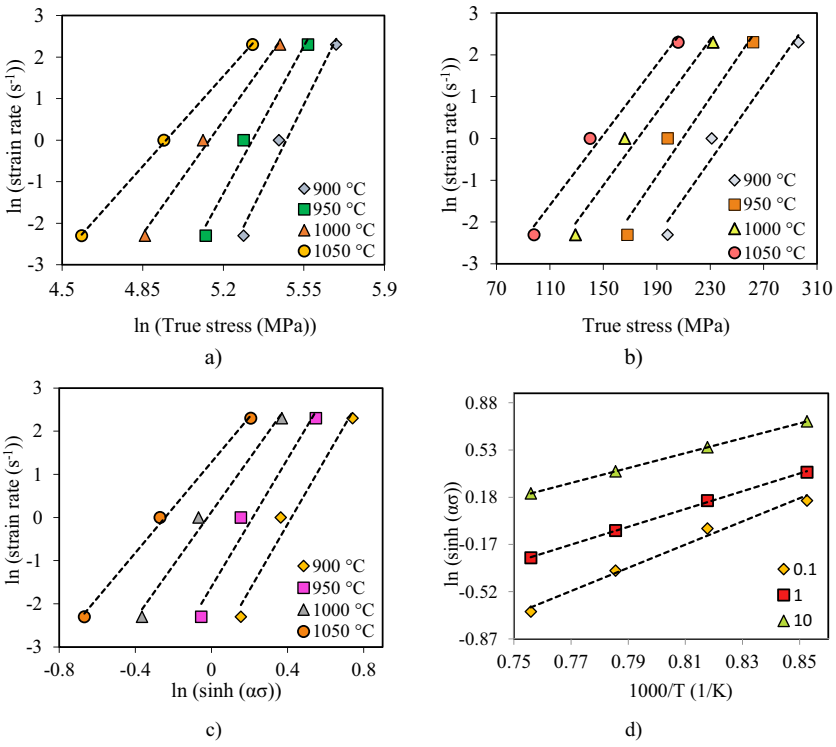

Fig. 6 Plots of **a**) ln (ε̇) against ln σ **b**) ln (ε̇) against σ **c**) ln (ε̇) against ln (sinh (α σ_{sat})) **d**) ln (sinh (α σ_{sat})) against 1000/T(1/K) for VG

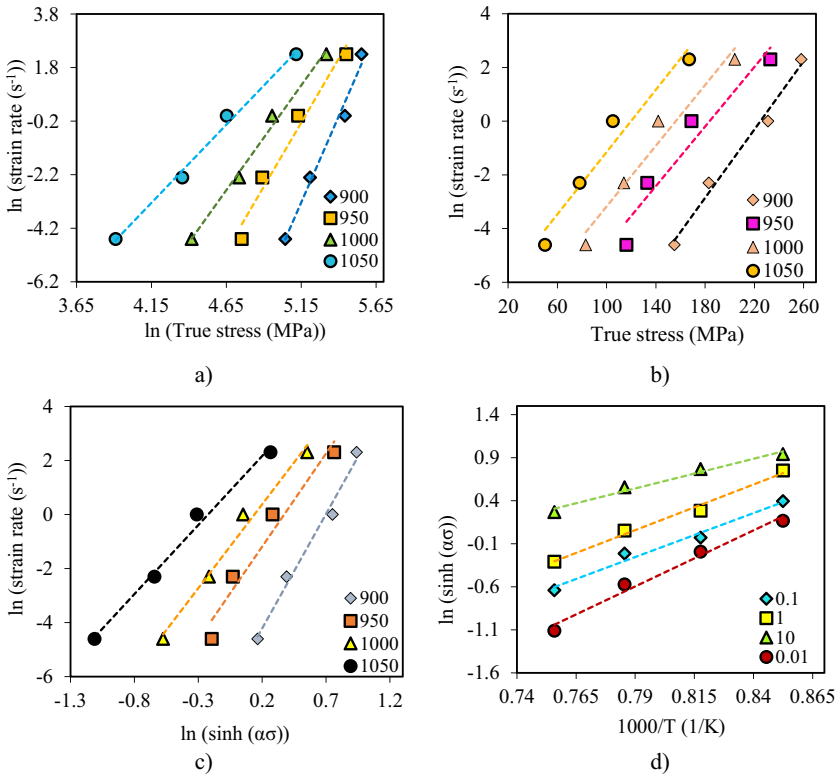

Fig. 7 Plots of **a**) ln (ε̇) against ln σ **b**) ln (ε̇) against σ **c**) ln (ε̇) against ln (sinh (α σ_{sat})) **d**) ln (sinh (α σ_{sat})) against 1000/T(1/K) for CE

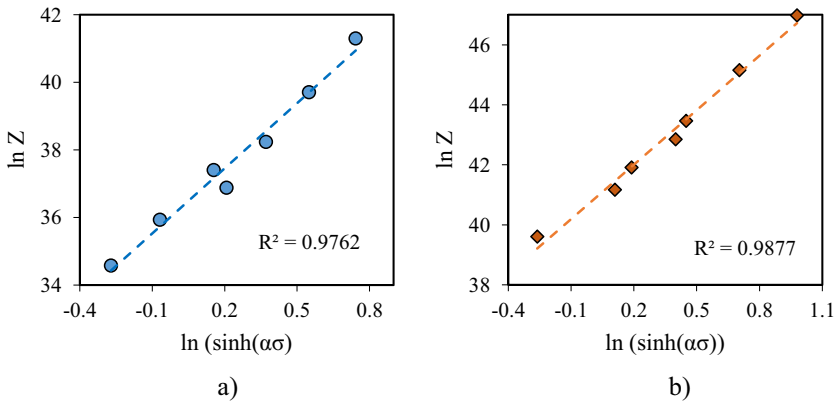

Fig. 8 The relationship between Ln Z against ln (sinh (ασ)) for **a**) VG and **b**) CE

Table 2 Constitutive constants and activation energy for VG and CE steels

X20 Steel	n'	β	η	a (MPa^{-1})	S	Q (kJmol^{-1})	A
VG	8.843	0.045	6.62	0.005	6.910	380.36	5.099×10^{15}
CE	7.787	0.046	5.79	0.006	9.047	435.70	2.977×10^{17}

3.2.3 Material constants for VG and CE steels

Table 2. shows the constitutive constants derived from modelled equations for the VG and CE steels. The stress exponent, n, and activation energy for hot working, Q are important parameters as they provide information on plastic deformation and underlying mechanisms controlling the process. The stress exponents of the two steels were analysed and the stress exponents obtained were VG (6.6), and CE (5.8). Studies by various authors [42, 44] have shown that a stress exponent value below 5 indicates the occurrence of DRX during hot deformation. Other reports [44–46] have

established that when the stress exponent is 5, the deformation process is controlled by the climb and glide dislocation mechanisms. Studies by Mirzadeh et al. [38] have suggested that in flow stress curves exhibiting DRV softening, dislocation climb and glide are the main controlling mechanisms. It is observed in Fig. 4 for VG and Fig. 5 for CE that the flow stress curves exhibit typical DRV flow softening behaviour. There are no peaks displayed followed by steady-state flow stress that is associated with DRX. It was therefore determined that the main deformation mechanism in the two steels was dislocation glide controlled by dislocation climb. A comparison of the stress exponents for the two steels showed a slight variation between the values for the VG and CE steels. The variation in the stress exponent values can be attributed to the differences in precipitation evolution during deformation for the two steels. Generally, the presence of carbides impedes motion of dislocations causing an increase in the stress exponent value [29]. Deformation at higher temperatures causes increased carbide dissolution hence, deformation occurring at the austenitic field may result in lower stress exponent values [46].

Apart from the stress exponent, the apparent activation energy for hot working is an indicator of mechanisms that control the deformation process. The activation energy obtained using Arrhenius equations does not represent the microstructural changes occurring during deformation [47]. It is therefore called 'apparent activation energy' as the equations assume the microstructure remains constant during deformation [44, 46]. The apparent activation energies obtained in this study were VG (380.36 $kJmol^{-1}$) and CE (435.7 $kJmol^{-1}$). These values differ greatly from the self-diffusion activation energy (Q_{SD}) of iron in austenite (270 $kJmol^{-1}$) and for α-Fe in ferrite (250 $kJ.mol^{-1}$) [29].

Wang et al. [48] described the deviation of activation energy from the imagined atomic mechanisms in terms of variation of temperature with Young's modulus [49]. McQueen and Ryan [43] explained that during hot working, the initial microstructure differs to some degree for different preheats and evolves quickly when testing. Other researchers have suggested that micro-alloying elements such as Cr and Mo play an important role as they increase the activation energy by solute drag effect and solid solution strengthening mechanisms [27, 49]. Further, the presence of precipitates, solutes, dispersoids, reinforcements, and inclusions also increases the activation energy by 50% [43].

As stated earlier, the activation energy is an indicator of the workability properties of a material during forming. It defines the level of resistance or difficulty to deformation a material poses to a hot working process. Comparisons of the activation energies of the two steels show, that VG steel was lower than CE. From the hot workability viewpoint, it suggests that VG steel had better workability compared to CE steel. The variation in activation energy between VG and CE may be ascribed to the variation in phase compositions during the deformation of the two steels.

The Phase compositions and precipitates influence the deformation process and therefore material constants. During hot deformation, material constants vary significantly with process parameters and the deformation temperature. The deformation temperature, in turn, influences the evolutions in microstructure and the resulting material flow stress. Flow stress directly affects the activation energy during hot deformation as flow stress increases with the activation energy for deformation [29].

The results of the apparent activation energies for the two steels indicate the energy required for initiating and maintaining the motion of dislocations within the crystals of the rejuvenation heat treatment CE steel was higher than that of the VG steel. It is concluded that the rejuvenation effect increased the materials' hot deformation resistance compared to that of the VG steel. The heat treatment CE steel would therefore have suitable application as recycled steel in an environment where resistance to plastic deformation at elevated temperatures would be desirable.

3.2.4 Constitutive models of the flow stresses

Using the saturated stresses obtained from stress–strain curves in the hyperbolic sine law; constitutive equations for the two steels are given as follows:

$$\text{VG } \dot{\varepsilon} = 5.0999 \times 10^{15}\left[\sinh(0.00503\sigma_{ss})\right]^{6.62}\exp\left[\frac{-380.361}{RT}\right] \tag{14}$$

$$\text{CE } \dot{\varepsilon} = 2.9774 \times 10^{17}\left[\sinh(0.00601\sigma_{ss})\right]^{5.79}\exp\left[\frac{-435.699}{RT}\right] \tag{15}$$

The material constants derived using the Arrhenius equations (Section 3.2.1) can model flow behaviour for the two steels using the Z parameter. From Equation (12), the solution of this equation gives Equation (16) [50] as:

$$\sigma = \frac{1}{\alpha}\ln\left\{\left(\frac{Z}{A}\right)^{1/n} + \left[\left(\frac{Z}{A}\right)^{2/n} + 1\right]^{1/2}\right\} \tag{16}$$

From Equation (13) the saturation flow stresses of VG and CE can be determined as follows:

$$\text{VG } \sigma = \frac{1}{0.005}\ln\left\{\left(\frac{Z}{5.099\times10^{15}}\right)^{\frac{1}{6.62}} + \left[\left(\frac{Z}{5.099\times10^{15}}\right)^{\frac{2}{6.62}} + 1\right]^{1/2}\right\} \tag{17}$$

$$\text{CE } \sigma = \frac{1}{0.006}\ln\left\{\left(\frac{Z}{2.977\times10^{17}}\right)^{\frac{1}{5.79}} + \left[\left(\frac{Z}{2.977\times10^{17}}\right)^{\frac{2}{5.79}} + 1\right]^{1/2}\right\} \tag{18}$$

3.2.5 Model validation

Verification of Equations (17) and (18) for the two steels (VG and CE) was done by comparison of flow stresses of the experimental and predicted data. The standard statistical parameters used to analyse the predictability of the equations were Pearson's correlation coefficient (Equation (19)) and Average Absolute Relative Error (AARE) (Equation (20)). Figure 9 ((a) and (b)) are plots of the experimental against predicted flow stresses obtained using Equations (17) and (18). The plots had a good correlation coefficient of 0.98 for the VG steel and 0.99 for the CE steel, where a value of 1.00 is a perfect correlation. The correlation coefficient method is however liable to bias towards high or low values therefore affecting the models' accuracy. The AARE statistical analysis method complements Pearson's correlation coefficient as it gives good accuracy and quantifies prediction deviation. In the AARE method, the calculation is through a term-by-term comparison of the relative error in the analysis of the developed equations. A lower AARE value signifies a higher accuracy of the constitutive model to predict the flow stresses and vice versa. The AARE values obtained were: VG (4.17%) and CE (9.01%). The AARE for VG indicated excellent predictability of the constitutive equation than CE. From the calculated parameters, the Arrhenius constitutive equation developed for the two steel has a high prediction accuracy of flow stress for all test conditions.

$$R = \frac{\sum_{i=1}^{N}(P_i - P)(E_i - E)}{\sqrt{\sum_{i=1}^{N}(P_i - P)^2}\sqrt{\sum_{i=1}^{N}(E_i - E)^2}} \tag{19}$$

$$AARE = \frac{1}{N}\sum_{i=1}^{N}\left|\frac{E_i - P_i}{E_i}\right| \times 100\% \tag{20}$$

where E_i is the experimental flow stress, Pi is the predicted flow stress obtained from constitutive equations, E and P, are mean flow stress values of experimental data E, P is the predicted data, and N is sum of the data points.

4 Conclusions

Hot deformation tests were studied for (VG) and heat-treated creep exhaust steel (CE) for a wide range of deformation conditions using a Gleeble® 3500 thermo-mechanical simulator. The outcomes of the investigation are as below:

1) The flow stress–strain curves of the CE steel, exhibited similar flow behaviour to the VG steel. In the initial deformation stages (strains < 0.2), work hardening (WH) controlled the deformation mechanisms for the two steels. At higher strains (> 0.2), the slopes of the flow stress curves reduced until the flow stress reached a steady-state flow stress owing to the flow-softening effect of DRV.
2) The stress exponent, n, for VG, was 6.62, and the CE steel was 5.79. The apparent activation energy, Q of VG steel was 380.36 kJ/mol, and for the rejuvenation, heat treatment CE steel was 435.70 kJ/mol. The rejuvenation effect on the apparent activation energy on the CE steel showed the steel to be harder to deform than the VG steel at elevated temperatures. This indicates that rejuvenation heat treatment can be used to restore creep exhaust X20 steel for reuse in thermal power plant components.
3) Two constitutive equations were developed for the two steels at a true strain of 0.6 as follows:
   i. For VG steel: $\dot{\varepsilon} = 5.0999 \times 10^{15}\left[\sinh(0.00503\sigma_{ss})\right]^{6.62}\exp\left[\frac{-380.36}{RT}\right]$
   ii. For CE steel: $\dot{\varepsilon} = 2.9774 \times 10^{17}\left[\sinh(0.00601\sigma_{ss})\right]^{5.79}\exp\left[\frac{-435.70}{RT}\right]$
4) The developed constitutive models were validated using standard statistical parameters: Pearson's correlation

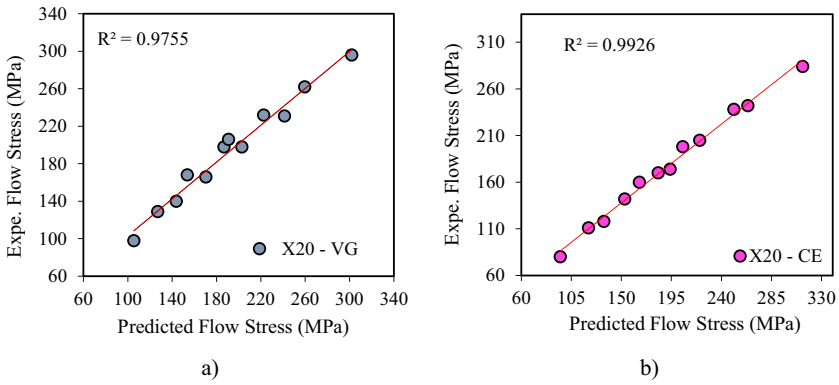

Fig. 9 Comparison of experimental and predicted flow stress for a) VG b) CE

coefficient (R) and the Average Absolute Relative Error (AARE). The R obtained for VG was 0.99, and AARE was 4.17%. For CE steel, R was 0.996, and AARE was 9.01%. The results established there was a good correlation between the experiment and predicted data.

Author contributions All authors contributed to the conceptualisation and design. Methodology and investigations were performed by Shem Maube, Japheth Obiko, Josias Van der Merwe, Fredrick Mwema, Desmond Klenam and Michael Bodunrin. The first draft of the manuscript was written by Shem Maube and all authors commented on previous versions of the manuscript. All authors read and approved the final manuscript.

Funding The authors declare that no funds, grants, or other support were received during the preparation of this manuscript.

Declarations

Competing interest The authors have no relevant financial or non-financial interests to disclose.

References

1. Skobir DA, Godec M, Jenko M, Markoli B (2008) Characterization of the carbides in the steel X20CrMoV12.1 used in thermal power plants. Surf Interface Anal 40(3–4):513–517. https://doi.org/10.1002/sia.2759
2. Pandey C, Mahapatra MM, Kumar P, Saini N (2018) Some studies on P91 steel and their weldments. J Alloys Compd 743:332–364. https://doi.org/10.1016/j.jallcom.2018.01.120
3. Bakic G, Zeravcic V, Djukic MB, Perunicic N (2014) Material characterization of the main steam gate valve made of X20CrMoV 12.1 steel after long term service. Procedia Mater Sci 3:1512–1517. https://doi.org/10.1016/j.mspro.2014.06.244
4. Hald J (2008) Microstructure and long-term creep properties of 9–12% Cr steels. Int J Press Vessel Pip 85(1–2):30–37. https://doi.org/10.1016/j.ijpvp.2007.06.010
5. Brózda J, Zeman M (2003) Wrong heat treatment of martensitic steel welded tubes caused major cracking during assembly of resuperheaters in a fossil fuel power plant. Eng Fail Anal 10(5):569–579. https://doi.org/10.1016/S1350-6307(03)00039-6
6. Salifu S, Desai D, Kok S (2021) Numerical simulation and creep-life prediction of X20 steam piping. Mater Today Proc 38(xxxx):893–898. https://doi.org/10.1016/j.matpr.2020.05.125
7. Barraclough DR, Gooch DJ (1985) Effect of inadequate heat treatment on creep strength of 12Cr–Mo–V steel. Mater Sci Technol (United Kingdom) 1(11):961–967. https://doi.org/10.1179/mst.1985.1.11.961
8. Danielsen HK, Hald J (2006) Behaviour of z phase in 9–12%Cr steels. Energy Mater Mater Sci Eng Energy Syst 1(1):49–57. https://doi.org/10.1179/174892306X99732
9. Danielsen HK (2016) Review of Z phase precipitation in 9–12 wt-%Cr steels. Mater Sci Technol (United Kingdom) 32(2):126–137. https://doi.org/10.1179/1743284715Y.0000000066
10. Hu ZF, Yang ZG (2003) Identification of the precipitates by TEM and EDS in X20CrMoV12.1 after long-term service at elevated temperature. J Mater Eng Perform 12(1):106–111. https://doi.org/10.1361/105994903770343556
11. Hald J (1996) Metallurgy and creep properties of new 9–12%Cr steels. Steel Res 67(9):369–374. https://doi.org/10.1002/srin.199605503
12. Yan W, Wang W, Shan YY, Yang K (2013) Microstructural stability of 9–12%Cr ferrite/martensite heat-resistant steels. Front Mater Sci 7(1):1–27. https://doi.org/10.1007/s11706-013-0189-5
13. Danielsen HK, Hald J (2009) On the nucleation and dissolution process of Z-phase Cr(V, Nb)N in martensitic 12%Cr steels. Mater Sci Eng A 505(1–2):169–177. https://doi.org/10.1016/j.msea.2008.11.019
14. Cipolla L, Danielsen HK, Venditti D, Di Nunzio PE, Hald J, Somers MAJ (2010) Conversion of MX nitrides to Z-phase in a martensitic 12% Cr steel. Acta Mater 58(2):669–679. https://doi.org/10.1016/j.actamat.2009.09.045
15. Cipolla L, Danielsen HK, Di Nunzio PE, Venditti D, Hald J, Somers MAJ (2010) On the role of Nb in Z-phase formation in a 12% Cr steel. Scr Mater 63(3):324–327. https://doi.org/10.1016/j.scriptamat.2010.04.025
16. Baldan A (1991) Rejuvenation procedures to recover creep properties of nickel-base superalloys by heat treatment and hot isostatic pressing techniques - A review. J Mater Sci 26(13):3409–3421. https://doi.org/10.1007/BF00557126
17. Lin S, Shen H, Zhou G, He W, Chen K (2022) A new rejuvenation heat treatment of crept Ni-based superalloy single crystals. IOP Conf Ser Mater Sci Eng 1249(1):012017. https://doi.org/10.1088/1757-899x/1249/1/012017
18. Falat L, Čiripová L, Homolová V, Džupon M, Džunda R, Koval K (2021)The effects of various conditions of short-term rejuvenation heat treatment on room-temperature mechanical properties of thermally aged P92 boiler steel. Materials (Basel) 14(20). https://doi.org/10.3390/ma14206076
19. Thomson RC, Bhadeshia HKDH (1992) Carbide precipitation in 12Cr1MoV power plant steel. Metall Trans A 23(4):1171–1179. https://doi.org/10.1007/BF02665048
20. Pandey C, Mahapatra MM, Kumar P, Saini N (2018) Homogenization of P91 weldments using varying normalizing and tempering treatment. Mater Sci Eng A 710(June 2017):86–101. https://doi.org/10.1016/j.msea.2017.10.086
21. Obiko J (2021) Friction correction of flow stress-strain curve in the upsetting process. IOP SciNotes 2(1):014401. https://doi.org/10.1088/2633-1357/abdd96
22. Li J et al (2022) Research on hot deformation behavior of F92 steel based on stress correction. Metals (Basel) 12(5):1–14. https://doi.org/10.3390/met12050698
23. Evans RW, Scharning PJ (2001) Axisymmetric compression test and hot working properties of alloys. Mater Sci Technol 17(8):995–1004. https://doi.org/10.1179/026708301101510843
24. Li Y, Onodera E, Chiba A (2010) Friction coefficient in hot compression of cylindrical sample. Mater Trans 51(7):1210–1215. https://doi.org/10.2320/matertrans.M2010056
25. Prasad YVRK, Rao KP (2008) Processing maps for hot deformation of rolled AZ31 magnesium alloy plate: Anisotropy of hot workability. Mater Sci Eng A 487(1–2):316–327. https://doi.org/10.1016/j.msea.2007.10.038
26. Xiao ZB, Huang YC, Liu Y (2016) Modeling of flow stress of 2026 Al alloy under hot compression. Adv Mater Sci Eng 2016:28–32. https://doi.org/10.1155/2016/3803472
27. Taylor AS, Hodgson PD (2011) Dynamic behaviour of 304 stainless steel during high Z deformation. Mater Sci Eng A 528(9):3310–3320. https://doi.org/10.1016/j.msea.2010.12.093
28. Ghosh S, Somani MC, Setman D, Mula S (2021) Hot deformation characteristic and strain dependent constitutive flow stress modelling of Ti + Nb stabilized interstitial free steel. Met Mater Int 27(8):2481–2498. https://doi.org/10.1007/s12540-020-00827-1

29. Obiko J, Chown L, Whitefield D, Bodunrin M (2022) Metal flow behaviour and processing maps of high heat resistant steel during hot compression. Int J Adv Manuf Technol 121(5–6):4153–4167. https://doi.org/10.1007/s00170-022-09577-3
30. Wang L, Liu F, Zuo Q, Chen CF (2013) Prediction of flow stress for N08028 alloy under hot working conditions. Mater Des 47:737–745. https://doi.org/10.1016/j.matdes.2012.12.074
31. Obiko J, Chown L, Whitefield D, Bodunrin M (2022) Understanding hot workability of power plant P92 creep resistant steels using dynamic material modelling (DMM) and microstructural evolution. Int J Interact Des Manuf. https://doi.org/10.1007/s12008-022-01084-9
32. Obiko J, Chown LH, Whitefield DJ (2019) Warm deformation behaviour of P92 steel. Mater Res Express 6(12). https://doi.org/10.1088/2053-1591/ab5e9c
33. Ge G, Zhang L, Xin J, Lin J, Aindow M, Zhang L (2018) Constitutive modeling of high temperature flow behavior in a Ti-45Al-8Nb-2Cr-2Mn-0.2Y alloy. Sci Rep 8(1). https://doi.org/10.1038/s41598-018-23617-7
34. Cai Z, Ji H, Pei W, Wang B, Huang X, Li Y (2019) Constitutive equation and model validation for 33Cr23Ni8Mn3N heat-resistant steel during hot compression. Results Phys. 15(July):102633. https://doi.org/10.1016/j.rinp.2019.102633
35. Jia L, Li Y, Zhang Y (2017) A Characterization for the deformation behavior of As-Cast P91 alloy steel and utilization in hot extrusion process. Adv Mater Sci Eng 2017. https://doi.org/10.1155/2017/6582739
36. Kumar N, Kumar S, Rajput SK, Nath SK (2017) Modelling of flow stress and prediction of workability by processing map for hot compression of 43CrNi steel. ISIJ Int 57(3):497–505. https://doi.org/10.2355/isijinternational.ISIJINT-2016-306
37. Nayan N et al (2021) Hot workability and microstructure control in Monel®400 (Ni–30Cu) alloy: An approach using processing map, constitutive equation and deformation modeling. Mater Sci Eng A 825(July):141855. https://doi.org/10.1016/j.msea.2021.141855
38. Mirzadeh H, Cabrera JM, Najafizadeh A (2011) Constitutive relationships for hot deformation of austenite. Acta Mater 59(16):6441–6448. https://doi.org/10.1016/j.actamat.2011.07.008
39. Laasraoui A, Jonas JJ (1991) Prediction of steel flow stresses at high temperatures and strain rates. Metall Trans A 22(7):1545–1558. https://doi.org/10.1007/BF02667368
40. Oudin A, Barnett MR, Hodgson PD (2004) Grain size effect on the warm deformation behaviour of a Ti-IF steel. Mater Sci Eng A 367(1–2):282–294. https://doi.org/10.1016/j.msea.2003.10.273
41. Alaneme KK, Babalola SA, Bodunrin MO (2021) On the prediction of hot deformation mechanisms and workability in Al6063/Nip and Al6063/steelp composites using hyperbolic-sine constitutive equation. Mater Today Proc 38(10):942–948. https://doi.org/10.1016/j.matpr.2020.05.463
42. Bodunrin MO (2020) Flow stress prediction using hyperbolic-sine Arrhenius constants optimised by simple generalised reduced gradient refinement. J Mater Res Technol 9(2):2376–2386. https://doi.org/10.1016/j.jmrt.2019.12.070
43. McQueen HJ, Ryan ND (2002) Constitutive analysis in hot working. Mater Sci Eng A 322(1–2):43–63. https://doi.org/10.1016/S0921-5093(01)01117-0
44. Zhou DQ, Xu XQ, Mao HH, Yan YF, Nieh TG, Lu ZP (2014) Plastic flow behaviour in an alumina-forming austenitic stainless steel at elevated temperatures. Mater Sci Eng A 594:246–252. https://doi.org/10.1016/j.msea.2013.11.021
45. Mirzadeh H (2015) Simple physically-based constitutive equations for hot deformation of 2024 and 7075 aluminum alloys. Trans Nonferrous Met Soc China (English Ed. 25(5):1614–1618. https://doi.org/10.1016/S1003-6326(15)63765-7
46. Carsí M, Peñalba F, Rieiro I, Ruano OA (2011) High temperature workability behavior of a modified P92 steel. Int J Mater Res 102(11):1378–1383. https://doi.org/10.3139/146.110603
47. El Wahabi M, Cabrera JM, Prado JM (2003) Hot working of two AISI 304 steels: A comparative study. Mater Sci Eng A 343(1–2):116–125. https://doi.org/10.1016/S0921-5093(02)00357-X
48. Wang S, Luo JR, Hou LG, Zhang JS, Zhuang LZ (2017) Identification of the threshold stress and true activation energy for characterizing the deformation mechanisms during hot working. Mater Des 113:27–36. https://doi.org/10.1016/j.matdes.2016.10.018
49. Baktash R, Mirzadeh H (2016) A simple constitutive model for prediction of single-peak flow curves under hot working conditions. J Eng Mater Technol Trans ASME 138(2). https://doi.org/10.1115/1.4032153
50. Mwema FM, Obiko JO, Mahamood RM, Adediran AA, Bodunrin MO, Akinlabi ET (2021) Constitutive analysis of hot forming process of P91 steel: finite element method approach. Adv Mater Process Technol 00(00):1–12. https://doi.org/10.1080/2374068X.2021.1939560

Publisher's Note Springer Nature remains neutral with regard to jurisdictional claims in published maps and institutional affiliations.

Springer Nature or its licensor (e.g. a society or other partner) holds exclusive rights to this article under a publishing agreement with the author(s) or other rightsholder(s); author self-archiving of the accepted manuscript version of this article is solely governed by the terms of such publishing agreement and applicable law.